RSC Advances

PAPER

View Article Online
View Journal | View Issue

Cite this: *RSC Adv.*, 2016, **6**, 68416

Enhancement of the photocatalytic activity of a TiO_2/carbon aerogel based on a hydrophilic secondary pore structure†

Hua'nan Cui,[a] Zhenxing Liang,[b] JinZhong Zhang,[c] Hong Liu[a] and Jianying Shi*[a]

Received 29th March 2016
Accepted 14th July 2016

DOI: 10.1039/c6ra08074j

www.rsc.org/advances

Improving the separation and utilization of electrons and holes in a photocatalytic process is a guarantee for high photocatalytic efficiency. We report a strategy to enhance the photocatalytic performance based on fabrication of a hydrophilic secondary pore structure by incorporating TiO_2 into a porous carbon aerogel (CA) with a 9.3 nm pore diameter, where TiO_2 resides on both the inner and outer surfaces of CA as evidenced by N_2 sorption isotherms and transmission electron microscopy. In such a structure, the spatial separation efficiency of photoelectrons and photoholes is supposed to get enhanced with interface electrons transferring into the inner surface of the pores *via* conductive CA. As a result, $HO^{\bullet}$ formation can be promoted in the confined inter surface of the hydrophilic secondary channel through O_2 reduction with the participation of photoelectrons and H_2O. And the remaining photoholes on the outer surface can oxidize water to generate $HO^{\bullet}$ as well. In contrast, TiO_2 is mainly dispersed on the outer surface of CA as small pore diameters of 3.4 and 4.3 nm; as a result, only uncombined photoholes on the outer surface contribute to $HO^{\bullet}$ generation *via* the water oxidation route. In line with this understanding, TiO_2/CA (9.3 nm) shows the largest amount of $HO^{\bullet}$ and thereby the highest efficiency of dimethyl phthalate degradation, as respectively evidenced by the electron paramagnetic resonance spectroscopy and the photocatalytic degradation test. These findings unveil the contribution of the surface/interface synergy effect on the separation and utilization of electrons and holes in photocatalytic process, and provide a potential strategy to enhance the photocatalytic performance.

Introduction

As an advanced oxidation process, photocatalytic degradation mediated *via* TiO_2 is an efficient method to eliminate organic pollutants from water. It has drawn much attention in the field of removing phthalate esters (PAEs) from an aqueous environment, because the end products after photocatalysis on PAEs are carbon dioxide, water, and inorganic mineral ions.[1–7] For TiO_2 photocatalysts, improving the separation and utilization of electrons and holes in photocatalytic processes is highly desired for high photocatalytic efficiency.[8] Surface modification,[9] sensitization[10] and transition-metal doping[11] are widely used strategies to optimize TiO_2 photocatalytic performance. In addition, assembling TiO_2 with carbon materials is another effective way,[12] as porous carbon support has been found to selectively accumulate reactants into its abundant pores[13–15] and its excellent conductivity serves to accelerate the separation of photogenerated carriers.[16–18] Some studies have suggested that such porous carbon powder is also capable of absorbing light, and the generated photoelectrons can be transferred to the conduction band of TiO_2 for further use.[19] Despite a large number of assemblies of TiO_2 with carbon were reported to data,[17,20–23] few systematic studies are undertaken to reveal the function of pore structure on photocatalytic performance, especially secondary pores with unique spatial features that are formed by encapsulating TiO_2 into carbon pore cavities. It has been reported that the unique pore-confined space can potentially play a vital role in enhancing catalytic activity and selectivity in heterogeneous catalysis.[24–26] Particularly, the CNT-confined TiO_2 exhibited improved visible-light activity as the modification of the electronic structure of TiO_2 induced by the unique confinement inside CNTs.[27]

Carbon aerogel (CA), possessing unique three-dimensional ultra-porous network with high porosity (80–98%), low electrical resistivity (≤40 mΩ cm), and large surface area (400–1100 cm^2 g^{-1}),[28,29] is a promising material in the application of processing contaminants.[28,30] In this work, three kinds of mesoporous CA

[a]*Key Laboratory of Environment and Energy Chemistry of Guangdong Higher Education Institutes, School of Chemistry and Chemical Engineering, Sun Yat-sen University, Guangzhou 510275, China. E-mail: shijying@mail.sysu.edu.cn*

[b]*Guangdong Provincial Key Laboratory of Fuel Cell Technology, School of Chemistry and Chemical Engineering, South China University of Technology, Guangzhou 510641, China*

[c]*Department of Chemistry and Biochemistry, University of California, Santa Cruz, CA 95064, USA*

† Electronic supplementary information (ESI) available: The thermogravimetry (TG), differential thermal gravity (DTG), X-ray diffraction and UV-vis absorption spectra for all samples. See DOI: 10.1039/c6ra08074j

with several nanometer pore diameters[31] were employed as support to assemble TiO_2/CA-*X* composite catalysts, where *X* denotes as the pore diameter of CA. Dimethyl phthalate (DMP), a member of phthalate acid esters (PAEs) detrimental to human being as endocrine disruptors, mutagens, reproductive and developmental toxicants,[7,32,33] was chosen as the target pollutant for evaluating the photocatalytic properties of the TiO_2/CA catalysts. Only TiO_2/CA-9.3 shows the enhanced photocatalytic activity, and TiO_2/CA-3.4 and TiO_2/CA-4.3 even gives the lower activity than bare TiO_2. It was found that the $HO^{\bullet}$ formation is correlated with the secondary pore structure of TiO_2/CA-*X*, and the contribution of surface/interface synergy effect on the separation and utilization of electrons and holes in the photocatalytic performance is discussed.

Results and discussion

Pore structure of TiO_2/CA-*X*

The pore structure of CA-*X* before and after assembling TiO_2 are investigated by N_2 adsorption–desorption isotherms, and the results are shown in Fig. 1a and b, respectively. The isotherms of CA-*X* and TiO_2/CA-*X* featured IV-type character with specific hysteresis loop at relatively high pressure, implying that both CA-*X* and TiO_2/CA-*X* are typical mesoporous materials. Fig. 2 shows the pore distribution of CA-*X* and TiO_2/CA-*X* samples calculated by a DFT model on ASiQwin software.[34,35] It can be seen that mesopores dominate the pore structure in both CA-*X* and TiO_2/CA-*X* samples with a small proportion of micropores and macropores. The detailed information of the pore structure is summarized in Table 1, *e.g.* pore volume, pore diameter and BET surface area.

The average pore diameters of three pristine CA samples are 3.1, 4.3 and 9.3 nm, as shown in Table 1. After assembling TiO_2, the pore diameters of CA-3.1 and CA-4.3 remain almost unchanged, but it decreases from 9.3 to 6.1 nm for CA-9.3. As seen in Table 1, both the volume of micropore (<2 nm) and mesopore (2–50 nm) and the BET surface of three TiO_2/CA-*X* samples decrease sharply when compared with those of the pristine CA-*X* samples. The decrease can be attributed to either the blockage of pore channels by TiO_2 dispersed on the carbon surface or the shrinkage of pore channels as TiO_2 was encapsulated into pore channels. The unchanged pore diameter of CA-3.1 and CA-4.3 indicates that TiO_2 was prominently dispersed on the outer surface of CA-3.1 and CA-4.3. While for CA-9.3, the dwindled 6.1 nm pore size suggests that, in addition to being dispersed on the outer surface, a considerable amount of TiO_2 was dispersed into the pore channels of CA-9.3. It is acknowledged that the capillary force is the driving force to infiltrate the precursor solution into the support channels during the preparation of supported catalysts,[36] which could account for the formation of secondary pore in TiO_2/CA-9.3. The 3.1 and 4.3 nm pore diameters of CA may be too small to allow the infiltrate of Ti precursor into the pore channel.

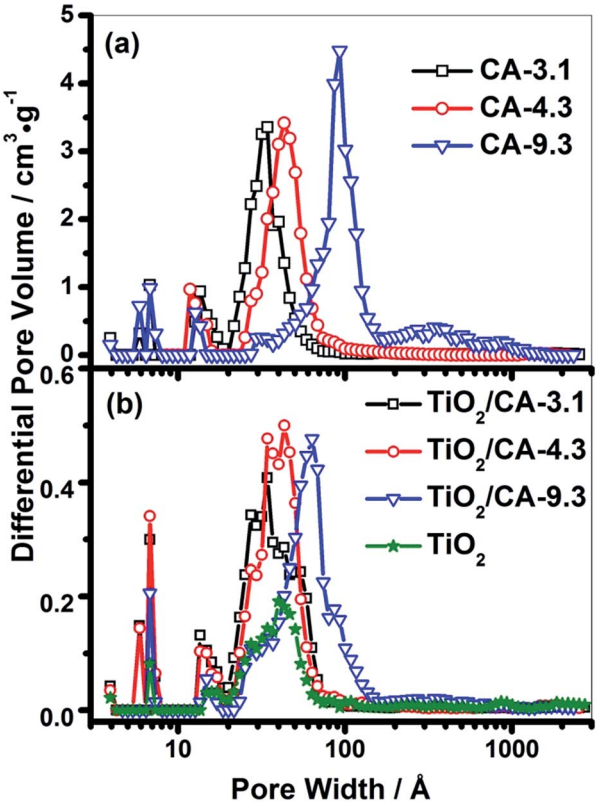

Fig. 2 Pore distribution of (a) CA-*X* and (b) TiO_2/CA-*X* and pure TiO_2.

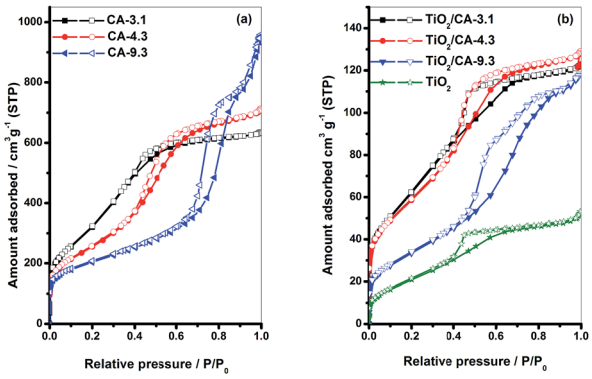

Fig. 1 N_2 adsorption–desorption isotherms of (a) CA-*X* and (b) TiO_2/CA-*X* and pure TiO_2.

Composition and structure of TiO_2/CA-*X*

The carbon content of TiO_2/CA-*X* samples was analyzed by thermogravimetry (TG) and differential thermal gravity (DTG) (Fig. S1†). The same loss steps at around 500 °C related to the carbon combustion indicate three samples possess the comparable carbon contents of about 15 wt% (Table 2), that is, the same amount of TiO_2 is dispersed on them. X-ray diffraction was used to determine the crystal structure of pristine TiO_2, TiO_2/CA-*X* and CA-*X*, and diffraction patterns are shown in Fig. S2.† A set of diffraction peaks related to anatase (PDF#21-1272) are observed in pristine TiO_2 and TiO_2/CA-*X*, in comparison, CA-*X* presents amorphous structure with broad diffraction patterns shown in insert of Fig. S2.† The results indicate that

Table 1 Pore parameters of carbon, TiO_2, and TiO_2/CA

Sample	D^a (nm)	$S_{BET}{}^b$ (m^2 g^{-1})	$V_{micro}{}^c + V_{meso}{}^d$ (cm^3 g^{-1})	DMP adsorption amount (mg g^{-1})
CA-3.1	3.1	1173	0.88	8.6 ± 0.4
CA-4.3	4.3	954	0.96	7.7 ± 0.5
CA-9.3	9.3	709	1.2	10.6 ± 0.6
TiO_2	4.4	84	0.07	0 ± 0.2
TiO_2/CA-3.1	3.8	237	0.17	6.4 ± 0.5
TiO_2/CA-4.3	4.1	215	0.18	6.2 ± 0.5
TiO_2/CA-9.3	6.1	124	0.17	4.4 ± 0.5

[a] Average mesopore size calculated form DFT method. [b] Brunauer–Emmett–Teller (BET) surface area calculated from adsorption branch of the N_2-sorption isotherm. [c] Micropore (<2 nm) volume calculated from cumulative pore volume of DFT method. [d] Mesopore (2–50 nm) volume calculated from cumulative pore volume of DFT method.

Table 2 Carbon content of TiO_2/CA-*X* samples

Sample	C content (%)	TiO_2 content (%)	C/TiO_2 ratio
TiO_2/CA-3.1	15.0	85.0	0.18 : 1
TiO_2/CA-4.3	14.9	85.1	0.18 : 1
TiO_2/CA-9.3	15.1	84.9	0.18 : 1

three TiO_2/CA-*X* samples possess the same TiO_2 crystal structure, irrespective of the pore diameter of CA.

The structure of CA-*X* before and after assembling TiO_2 was further studied by TEM and HRTEM, and the representative images of these samples are shown in Fig. 3. It can be seen that both CA-4.3 (Fig. 3a) and CA-9.3 (Fig. 3c) exhibit disordered wormhole-like mesopore structures, which are consistent with the previous report.[31] After assembling TiO_2 on CA-4.3 (Fig. 3b), abundant and spherical domains (marked in the dash line frame) on several nanometer scale with clear lattice fringes of TiO_2 are disorderly dispersed on the surface of CA-4.3. When comparing CA-9.3 (Fig. 3c) *vs.* TiO_2/CA-9.3 (Fig. 3d), the pore channels of CA-9.3 are partially filled by the assembled TiO_2, deduced from the variation on contrast of the two images. In addition, TiO_2 particles (marked in the dash line frame) with identifiable lattice fringes are observed on the edge of CA-9.3 without serious aggregation. The TEM results further confirm that TiO_2 is dispersed on outer surface of CA-4.3, while on both inner and outer surfaces of CA-9.3, which are consistent with the pore structure analysis (*vide supra*).

Effect of porous structure and wettability on DMP adsorption

The DMP adsorption on TiO_2/CA-*X* is evaluated by kinetic adsorption curves in Fig. 4, and the one-hour absorption amount is listed in Table 1. CA-3.1 and CA-4.3 present the similar adsorption behaviors (dashed line) with *ca.* 8 mg g^{-1} DMP amount upon one-hour absorption, which is less than the amount of 10 mg g^{-1} on CA-9.3. After assembling TiO_2, DMP adsorption on three TiO_2/CA-*X* samples (solid lines) decreases in different levels compared with each pristine CA-*X*. It decreases from 10 to 4 mg g^{-1} when comparing CA-9.3 with TiO_2/CA-9.3, and from *ca.* 8 to 6 mg g^{-1} upon assembling TiO_2 on CA-3.1 or CA-4.3. It was reported the volume of mesopores and micropores determined the adsorption of organic micro pollutants, such as microcystins by activated carbons.[37,38] The total volume of micropores and mesopores for CA-3.1, CA-4.3 and CA-9.3 (listed in Table 1) is about 0.88, 0.96 and 1.2 cm^3 g^{-1}, respectively. The volume data well accounts for the similar DMP adsorption capacities of CA-3.1 and CA-4.3 and the highest adsorption amount of CA-9.3. After assembling TiO_2 on CA-*X*, the total volume of all three samples decreases significantly to the same level of ~0.17 cm^3 g^{-1}, as presented in Table 1. The volume decrease of all three samples are consistent with their adsorption amount decrease, but the comparable 0.17 cm^3 g^{-1} total volume cannot explain their different adsorption capacity, *e.g.* 4 mg g^{-1} in TiO_2/CA-9.3 and the 6 mg g^{-1} in TiO_2/CA-3.1 and TiO_2/CA-4.3.

In addition to pore volume, the wettability of adsorbent also plays a vital role on its absorption performance, for example, the hydrophilic TiO_2 possesses the negligible DMP adsorption in Fig. 4. Fig. 5 presents the contact angle results and the droplet images of all samples as well. It can be seen that all CA-*X* samples are hydrophobic with apparent contact angles over 120°. After loading hydrophilic TiO_2 with a contact angle of less than 10°, all samples change to be hydrophilic accompanying with the decrease of contact angles. Notably, TiO_2/CA-9.3 shows the smallest contact angle *ca.* 70° in three TiO_2/CA-*X* samples, which is consistent with its unique pore structure that hydrophilic TiO_2 was dispersed on both inner and outer surface of CA-9.3. The hydrophilic nature of TiO_2/CA-9.3 enables it to be more inclined to adsorb H_2O but not DMP. Thus, TiO_2/CA-9.3 gives the lowest DMP adsorption amount, as shown in Table 1.

Photocatalytic degradation of DMP

DMP was chosen as the target pollutant to study the influence of pore structure on the photocatalytic activities of TiO_2/CA-*X* samples. It should be noted that no DMP degradation occurred when irradiating TiO_2/CA-*X* photocatalysts with visible light ($\lambda >$ 420 nm). As previous reports,[39,40] the photodegradation process in our case occurs with UV-light irradiation of photocatalysts and carbon does not sensitize TiO_2, though the visible absorption related to carbon is observed in UV-vis absorption spectra (Fig. S3†).

Fig. 6 shows the dynamic curves of DMP photocatalytic degradation during 3 hours. It can be seen that TiO_2/CA-9.3 gives the highest degradation efficiency of 83%, and TiO_2 shows the secondary degradation efficiency *ca.* 70%. TiO_2/CA-3.1 and TiO_2/CA-4.3 respectively exhibit the third and fourth degradation efficiency of 55% and 44%, which are followed by the mechanical mixture of TiO_2 and CA-9.3 with 25% efficiency.

The intermediates in DMP degradation process are identified from positive modes of MS (Fig. S4†). The signal at m/z = 195 (+H) which belongs to DMP has been strongly weakened and two major intermediates were formed according to the signals in the mass spectra. The signals at m/z = 149 (+H) and 171 (+Na) might belong to *o*-phthalic anhydride. The signal at m/z = 167 (+H) might be phthalic acid. The similar intermediates were observed by Wang *et al.*[3]

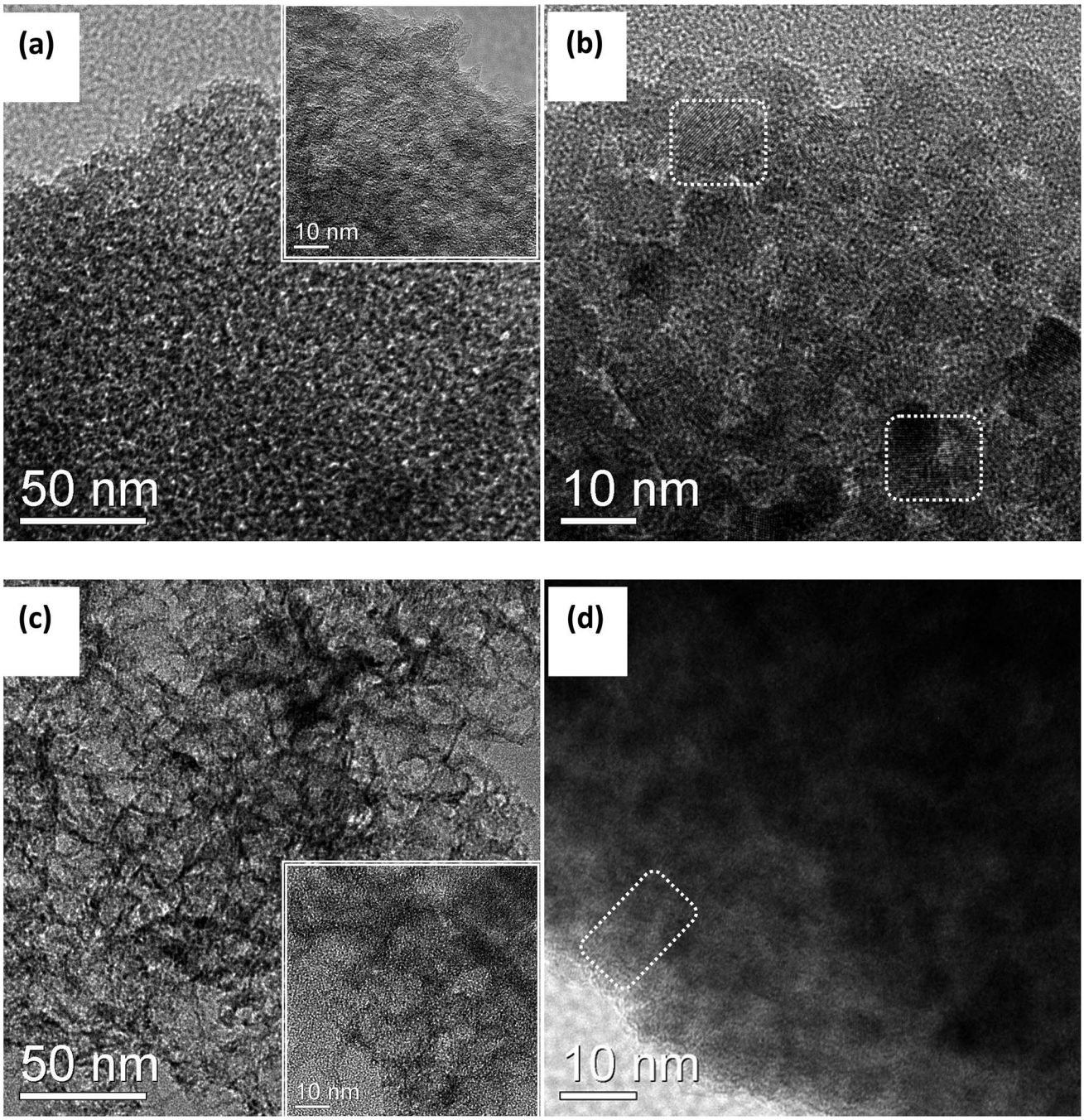

Fig. 3 HRTEM images of (a) CA-4.3, (b) TiO_2/CA-4.3, (c) CA-9.3, and (d) TiO_2/CA-9.3.

Photocatalytic activity is acknowledged to rely on the adsorption capacity of organic molecules upon photocatalyst, and high adsorption capacity is favorable for the photocatalytic degradation due to the accumulation of organic molecules and the intermediates, if any.[41] However, in our case, the high adsorption amount of DMP in TiO_2/CA-3.1 and TiO_2/CA-4.3 did not result in high degradation efficiency. TiO_2/CA-9.3, which has lowest adsorption amount of DMP, presents the highest degradation efficiency. That is, the DMP accumulation in TiO_2/CA-*X* relying on the adsorption capacity is unessential for its photodegradation in this case.

In consideration of the similar absorption features of TiO_2/CA-X in UV-vis absorption spectra (Fig. S3†), the amounts of photogenerated carriers in these samples are comparable, which cannot account for such a big difference in photodegradation efficiency (see Fig. 6) as well. The $HO^{\bullet}$ was further studied to address the difference in DMP degradation efficiency. Fig. 7 gives the EPR spectra of DMPO-OH adduct produced by *in situ* illuminating aqueous solutions respectively containing TiO_2, TiO_2/CA-9.3 and TiO_2/CA-3.1. The control experiment result of DMPO aqueous solution is also shown in Fig. 7. It can be seen that TiO_2/CA-9.3 exhibits the largest

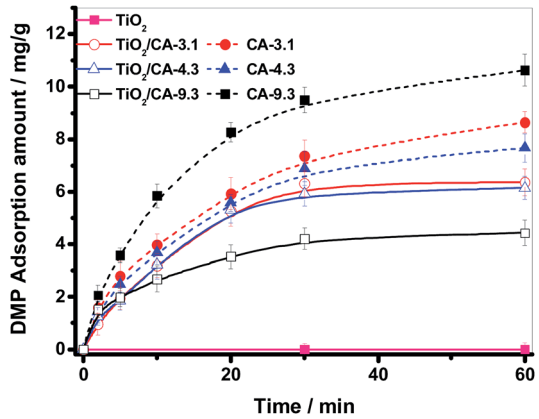

Fig. 4 The adsorption curves for DMP onto CA-*X*, TiO_2/CA-*X*, and pristine TiO_2.

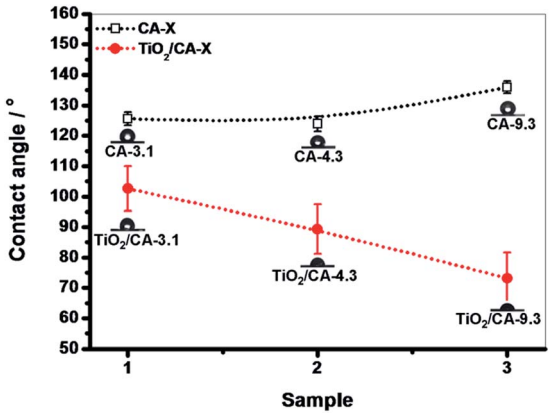

Fig. 5 Contact angle and droplet images of CA-*X* and TiO_2/CA-*X*.

amount of HO$^\bullet$, TiO_2 gives the secondary HO$^\bullet$ amount, and TiO_2/CA-3.1 shows the lowest HO$^\bullet$ amount. This order of HO$^\bullet$ amount is consistent with the DMP degradation sequence in Fig. 6. It was reported that water treatment processes was highly dependent on hydroxyl radical and it is critical to maximize hydroxyl radical generation during TiO_2 photocatalysis.[4] In light of above MS results, the major intermediates should be formed by the attack of hydroxyl radicals on the alkyl chains of DMP. Therefore, we focus on the formation of HO$^\bullet$ to correlate the structures of TiO_2/CA-*X* with their photocatalytic properties hereinafter.

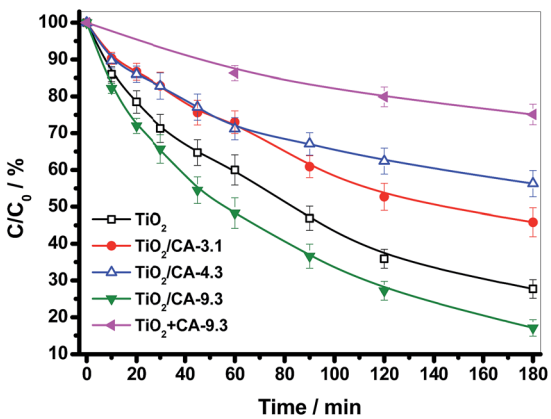

Fig. 6 Dynamic curves of photocatalytic degradation DMP with TiO_2/CA-*X*, TiO_2 and TiO_2 + CA-9.3.

The mechanism of photocatalytic degradation

A typical photocatalytic process begins with the light absorption to produce electrons and holes (eqn (1)). The photogenerated holes are consumed by the oxidization of H_2O to produce active HO$^\bullet$ (eqn (5));[42] meanwhile, the photoelectrons are consumed by O_2 reduction to $^\bullet O^{2-}$ (eqn (2)), followed by the generation (eqn (3)) and decomposition (eqn (4)) of H_2O_2, in which process active HO$^\bullet$ is also generated. It is noted that active HO$^\bullet$ with strong oxidation ability leads to the fast degradation of organic molecules (eqn (6)).[43]

$$TiO_{2(surface)} + h\nu \rightarrow e_{CB}^- + h_{VB}^+ \quad (1)$$

$$e_{CB}^- + O_2 \rightarrow {}^\bullet O_2^- \quad (2)$$

$$^\bullet O_2^- + H_2O \rightarrow H_2O_2 \quad (3)$$

$$H_2O_2 \rightarrow HO^\bullet + OH^- \quad (4)$$

$$H_2O + h_{VB}^+ \rightarrow HO^\bullet + H^+ \quad (5)$$

$$HO^\bullet + C_{10}H_{10}O_4 \rightarrow H_2O + CO_2 \quad (6)$$

In above processes, there are two ways for HO$^\bullet$ formation: H_2O oxidation in eqn (5) and O_2 reduction with the participation of H_2O in eqn (2)–(4). Most important of all, in both ways, H_2O molecule is indispensable for HO$^\bullet$ formation. Thus, the more hydrophilic surface in TiO_2/CA-9.3 can account for its higher HO$^\bullet$ generation ability than that of TiO_2/CA-3.1 with hydrophobic surface. However, it is still puzzling that the HO$^\bullet$ amount produced in TiO_2/CA-9.3 is even larger than that in pristine TiO_2, concerning the super-hydrophilic TiO_2 *vs.* hydrophilic TiO_2/CA-9.3. We propose that a structure-related effect exists in TiO_2/CA-

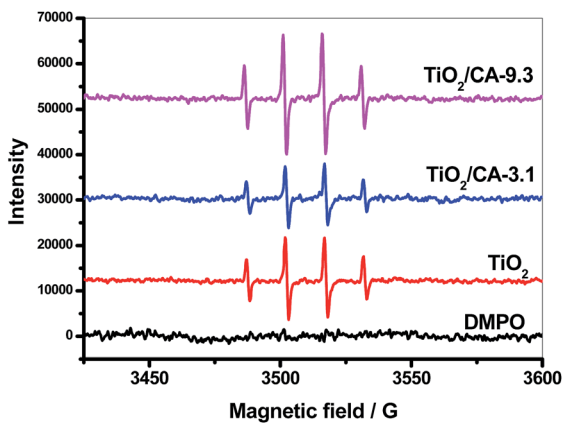

Fig. 7 EPR spectra of DMPO-OH adduct in aqueous solution respectively containing TiO_2, TiO_2/CA-9.3 and TiO_2/CA-3.1 illuminating with Xe lamp.

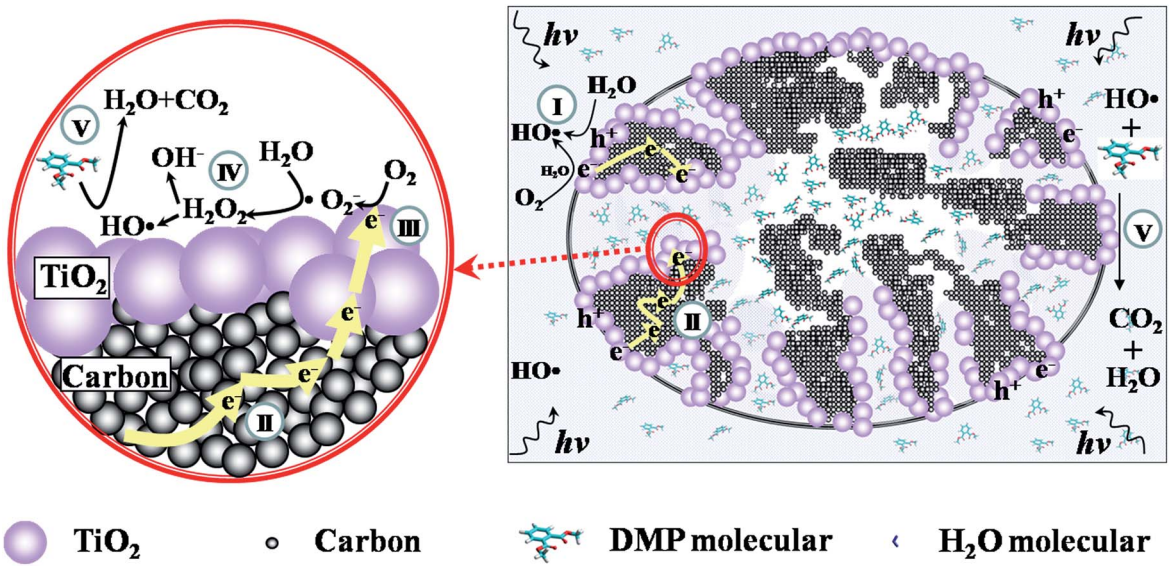

Fig. 8 Schematic illustration of DMP degradation in TiO_2/CA-9.3 under light irradiation. The red ring describes the reactions occurring in the secondary pores. The processes include: (I) on the external surface, HO• formation with H_2O reduction and oxidation, (II) the photoelectrons generated on external surface migrates to the internal surface through the carbon layer, (III) on the internal surface, the photoelectrons are trapped by O_2 to produce $\bullet O^{2-}$, (IV) HO• are generated with the participation of H_2O and $\bullet O^{2-}$, (V) DMP is oxidized by active HO• on both external and internal surface.

9.3 toward HO• generation and the mechanism of HO• formation on the outer and inner surfaces of TiO_2/CA-9.3 is illustrated in Fig. 8 (*vide infra*).

It is understandable that the primary factor inhibiting HO• formation *via* either the oxidation way (eqn (5)) or reduction way (eqn (2)–(4)) is the recombination of photoholes and photoelectrons in the photodegradation process. With respect to the special structure of TiO_2/CA-9.3 with TiO_2 dispersed on both inner and outer surfaces, it is possible that the photoelectrons generated on the outer surface transfer to its inner surface through the conductive CA (process II in Fig. 8). This process potentially increases the separation efficiency of photoelectrons and photoholes. As a result, HO• formation *via* H_2O oxidation with photoholes (eqn (5)) is enhanced on the outer surface TiO_2 (process I in Fig. 8). Meanwhile, the formation of HO• *via* O_2 reduction with participation of H_2O and photoelectrons (eqn (2)–(4)) is improved in the hydrophilic secondary channels of TiO_2/CA-9.3 (process IV in Fig. 8 amplifying red-circle region), because in this secondary channels the three integral components of photoelectrons, O_2 and H_2O needed for HO• formation are simultaneously satisfied with the photoelectrons transfer aforementioned, air bubbling in aqueous solution, and surface hydrophilic property, respectively. In addition, the spatial confinement effect[44,45] arising from narrower secondary channel further facilitates the HO• formation by stabilizing the intermediates of $\bullet O^{2-}$ and H_2O_2. In summary, the interface electron transfer between TiO_2 and CA-9.3 promotes the spacial separation of photoelectrons and photoholes, and hydrophilic secondary-pore surface with confined space results in the increase of HO• formation possibility in reduction way (eqn (2)–(4)), and thereby leads to the highest DMP degradation activity of TiO_2/CA-9.3 (process V in Fig. 8).

Comparing with TiO_2/CA-9.3 with uniform distribution of TiO_2 on both outer and inner surface of CA-9.3 support, prepared by introducing CA-9.3 into titanium precursor solution prior to sol–gel formation, TiO_2 + CA-9.3 is a simply mixture of TiO_2 and CA-9.3 and no hydrophilic porous structure exists, in addition, part of CA-9.3 covering on TiO_2 could block the incident light by its self-absorption. Therefore, the degradation activity of TiO_2 + CA-9.3 is far lower than TiO_2/CA-9.3, even lower than TiO_2/CA-3.1 and TiO_2/CA-4.3, where TiO_2 mainly dispersed on the outer surface of CA supports as their small pore diameter.

Conclusions

TiO_2/CA-*X* photocatalysts with variable pore structures were fabricated and the correlation between the pore structure and the photocatalytic property was systematically studied. Our date indicates that dispersion of TiO_2 on CA-*X* relies on the pore diameter of CA support. The large diameter enables TiO_2 to be dispersed on both inner and outer surface of CA support, accompanying with the formation of the secondary pore with narrower channel. This special porous structure of TiO_2/CA-9.3 leads to the separation of electrons and holes in space in the photocatalytic process. Correspondingly, the two routes of HO• formation in H_2O oxidation and O_2 reduction with participation of H_2O are promoted. The largest amount HO• finally causes the highest DMP degradation efficiency in TiO_2/CA-9.3. It was concluded that the surface/interface synergy effect plays a positive role on the spatial separation and utilization of electrons and holes in photocatalytic process, which suggests a potential strategy for designing high efficiency photocatalysts.

Experimental

Materials

Titanium(IV) isopropoxide (95%) and tetraethyl orthosilicate (TEOS, 98%) were purchased from Aladdin (Shanghai, China). Other reagents used were all analytical reagents and purchased from Guangzhou Chemical Reagent Plant (Guangzhou, China). All reagents were used as received without further purification, and the double distilled water was used in all experiments.

Preparation

The carbon aerogels were synthesized following a previously published procedure.[31] Briefly, the raw materials of glucose (2 g), tetraethyl orthosilicate (TEOS, 3 mL) and sulfuric acid (H_2SO_4) solution (4 mL, pH = 2) were mixed and stirred until a homogenate was formed. The mixture was then treated by hydrofluoric acid (HF, 4 wt%) under stirring, gelated, and aged in a plastic bottle as follows: 40 °C for 2 days, followed by 100 °C for 6 h, and finally 160 °C for 6 h. The xerogel was subsequently carbonized in nitrogen atmosphere at 900 °C for 3 h, and washed by 40 wt% HF to remove silica. The HF/TEOS molar ratio used was 0, 1/30 and 1/7, and as a result, the pore diameters were controlled by changing the amount of HF during the sol–gel process of TEOS. The notation of "CA-*X*" is used to denote the samples, with *X* being the pore diameter of CA calculated by the density function theory (DFT) model. The TiO_2/CA-*X* sample was synthesized with CA-*X* as the support material.

TiO_2/CA-*X* samples were prepared by a sol–gel method with titanium isopropoxide as Ti source. A typical procedure is as follows. Titanium(IV) isopropoxide (3 mL) was introduced into ethanol (20 mL) with vigorous stirring for 30 min, and then concentrated nitric acid (0.16 mL) was added into this solution. After stirring for 5 minutes, CA (0.16 g) was distributed into this solution. The mixture solution was constantly stirred until a homogenous CA-contained gel was formed. The gel was aged in air to form a ergoes, which was then ground into fine powder. The powder was calcined at 400 °C for 5 h in the nitrogen atmosphere, and TiO_2/CA-*X* samples were thus obtained. For comparison, pure TiO_2 was also prepared following the same procedure in the absence of CA. Mechanically mixed TiO_2 and CA-*X* sample with the same mass ratio as TiO_2/CA-*X* samples, marked as TiO_2 + CA-9.3 was also prepared.

Characterization

The crystalline structures of TiO_2/CA-*X* samples were analyzed by D8 Advance X-ray Diffractometer (XRD, Bruker, D8 advance, Germany) with Cu-Kα radiation source at scanning rate of 10 min^{-1}. The morphologies of TiO_2/CA-*X* samples were observed by transmission electron microscope (TEM, JEOL, JEM-2100, Japan) on a JEM 2100F 200 kV field emission transmission electron microscope. The carbon content in TiO_2/CA-*X* samples was determined by thermogravimetry analysis (TG, Netzsch, TG209, Germany) in air atmosphere. The pore structures of samples were probed by N_2 adsorption–desorption isotherm at 77 K (Quantachrome, AutosorbiQ, American). Before measurement, the samples were out-gassed at 200 °C for 12 h. The specific surface area was determined by Brunauer–Emmett–Teller (BET) model, while the pore size and volume were calculated by density functional theory (DFT) method on Quantachrome ASiQwin software. Diffuse reflection spectra (DSR) were recorded on UV-vis spectrophotometer (Shimadzu, UV-3150, Japan, equipped with an integrating sphere) to study the optical properties of the samples.

Electron Paramagnetic Resonancse spectrometer (EPR, Bruker, A 300, Germany) were used to detect the hydroxyl radical with 5,5-dimethy-1-pyrroline-N-oxide (DMPO, Sigma-Aldrich) as the radical trap. The samples were irradiated with xenon arc source system (LOT Oriel 75-150, UK). Data acquisition parameters were as follows: magnetic field, 3514 G; microwave power, 5.95 mW; modulation frequency, 100 kHz; modulation amplitude, 1.00 G; microwave frequency, 9.86 GHz; sweep time, 20.48 s. The hydrophilic properties of CA-*X* and TiO_2/CA-*X* were measured by OCA contact angle system (Dataphysics, OCA20, Germany). The intermediates in the degradation process were identified from positive modes of MS (AB Sciex, triple QuadTM 4500).

Adsorption and photocatalytic degradation of DMP

Dimethyl phthalate (DMP, 2 mg L^{-1}) was chosen as the model target to investigate the photocatalytic properties of porous TiO_2/CA-*X* samples. Prior to the photocatalytic reaction, the adsorption experiment of DMP on TiO_2/CA-*X* was carried out in dark at room temperature by adding 0.01 g of TiO_2/CA-*X* sample into 100 mL 2 mg L^{-1} DMP aqueous solution. The photodegradation experiments were carried out in a cylindrical glass reactor (Φ 9.0 cm × 10.6 cm) covered by a cylindrical quartz vessel (Φ 9.0 cm × 9.0 cm), which was full-filled with double distilled water to remove the infrared light radiated from 300 W Xe lamp (Changtuo, PLS-SXE 300/300 UV, Beijing). The light intensity was 85 mW cm^{-2} determined by a radiometer (FZ-A, Photoelectric Instrument factory of Beijing Normal University). The emission spectrum of the Xe lamp has been reported in ref. 8. For a typical photocatalytic experiment, 0.1 g L^{-1} of TiO_2/CA-*X* catalysts were firstly pre-adsorbed with 100 mL 2 mg L^{-1} DMP in dark before irradiation to establish adsorption–desorption equilibrium. Then photocatalytic experiments were initiated by air bubbling and irradiation. During the experiments, 0.5 mL of solution was sampled at preset time interval for the analysis of the concentration of DMP by high performance liquid chromatography (HPLC, Techcomp, LC2130, Shanghai, China) equipped with a reverse phase column (Waters, XT erra MS C-18, 5 μm) and a UV detector. The mobile phase was composed of 50% acetonitrile and 50% water, and the detection wavelength was 276 nm. For comparison, pristine TiO_2 and mechanical mixtures of TiO_2 and CA-9.3 (TiO_2 + CA) were also tested under the same condition. The amount of TiO_2 was to the same as that in TiO_2/CA-*X*.

Acknowledgements

The research was financially supported by the 973 Program (2014CB845600), NSFC (No. 21103235), NSF of Guangdong Province (No. S2012010010775), the Key Laboratory of Fuel Cell Technology of Guangdong Province, and the Key Laboratory of Environmental Pollution Control and Remediation Technology of Guangdong Province (No. 2011K0011). JZZ is grateful to the BES Division of the US DOE for financial support.

References

1 Y. C. Chung and C. Y. Chen, *Water, Air, Soil Pollut.*, 2009, **200**, 191–198.
2 Y. H. Chen, L. L. Chen and N. C. Shang, *J. Hazard. Mater.*, 2009, **172**, 20–29.
3 W. C. Liao and P. Wang, *J. Braz. Chem. Soc.*, 2009, **20**, 866–872.
4 W. J. Jiang, J. A. Joensa, D. D. Dionysiou and K. E. O' Shea, *J. Photochem. Photobiol., A*, 2013, **262**, 7–13.
5 Z. J. Huang, P. X. Wu, Y. H. Lu, X. R. Wang, N. W. Zhu and Z. Dang, *J. Hazard. Mater.*, 2013, **246–247**, 70–78.
6 Y. Jing, L. S. Li, Q. Y. Zhang, P. Lu, P. H. Liu and X. H. Lu, *J. Hazard. Mater.*, 2011, **189**, 40–47.
7 L. Xu, X. Yang, Y. H. Guo, F. Y. Ma, Y. N. Guo, X. Yuan and M. X. Huo, *J. Hazard. Mater.*, 2010, **178**, 1070–1077.
8 J. Y. Shi, H. N. Cui, Z. X. Liang, X. H. Lu, Y. X. Tong, C. Y. Su and H. Liu, *Energy Environ. Sci.*, 2011, **4**, 466–470.
9 D. Zhao, C. C. Chen, Y. F. Wang, H. W. Ji, W. H. Ma, L. Zang and J. C. Zhao, *J. Phys. Chem. C*, 2008, **112**, 5993–6001.
10 S. G. Bairu, E. Mghanga, J. Hasan, S. Kola, V. J. Rao, K. Bhanuprakash, L. Giribabu, G. P. Wiederrecht, da. R. Silva, L. G. C. Rego and G. Ramakrishna, *J. Phys. Chem. C*, 2013, **117**, 4824–4835.
11 M. Garcia-Mota, A. Vojvodic, F. Abild-Pedersen and J. K. Norskov, *J. Phys. Chem. C*, 2013, **117**, 460–465.
12 R. Leary and A. Westwood, *Carbon*, 2011, **49**, 741–772.
13 C. Pelekani and V. L. Snoeyink, *Water Res.*, 1999, **33**, 1209–1219.
14 X. W. Zhang, M. H. Zhou and L. Lei, *Carbon*, 2005, **43**, 1700–1708.
15 Y. H. Ao, J. J. Xu, D. G. Fu, X. W. Shen and C. W. Yuan, *Colloids Surf., A*, 2008, **312**, 125–130.
16 H. Zhang, X. J. Lv, Y. M. Li, Y. Wang and J. H. Li, *ACS Nano*, 2010, **4**, 380–386.
17 H. Y. Ng, S. Ikeda, M. Matsumura and R. Amal, *Energy Environ. Sci.*, 2012, **5**, 9307–9318.
18 W. D. Wang, C. G. Silva and J. L. Faria, *Appl. Catal., B*, 2007, **70**, 470–478.
19 W. Wei, C. Yu, Q. F. Zhao, G. S. Li and Y. Wan, *Chem.–Eur. J.*, 2013, **19**, 566–577.
20 Y. Yao, G. Li, S. Ciston, R. M. Lueptow and K. A. Gray, *Environ. Sci. Technol.*, 2008, **42**, 4952–4957.
21 X. H. Xia, Z. H. Jia, Y. Yu, Y. Liang, Z. Wang and L. L. Ma, *Carbon*, 2007, **45**, 717–721.
22 L. Gu, Z. X. Chen, C. Sun, B. Wei and X. Yu, *Desalination*, 2010, **263**, 107–112.
23 M. F. Wu, Y. N. Jin, G. H. Zhao, M. F. Li and D. M. Li, *Environ. Sci. Technol.*, 2010, **44**, 1780–1785.
24 D. Wang, G. H. Yang, Q. X. Ma, M. B. Wu, Y. S. Tan, Y. Yoneyama and N. Tsubaki, *ACS Catal.*, 2012, **2**, 1958–1966.
25 H. Q. Yang, L. Zhang, L. Zhong, Q. H. Yang and C. Li, *Angew. Chem., Int. Ed.*, 2007, **46**, 6861–6865.
26 Z. J. Chen, X. H. Li and C. Li, *Chin. J. Catal.*, 2011, **32**, 155–161.
27 W. Chen, Z. L. Fan, B. Zhang, G. J. Ma, K. Takanabe, X. X. Zhang and Z. P. Lai, *J. Am. Chem. Soc.*, 2011, **133**, 14896–14899.
28 Y. N. Jin, M. F. Wu, G. H. Zhao and M. F. Li, *Chem. Eng. J.*, 2011, **168**, 1248–1255.
29 J. M. Miller and B. Dunn, *Langmuir*, 1999, **15**, 799–806.
30 H. D. Du, L. Gan, B. H. Li, P. Wu, Y. L. Qiu, F. Y. Kang, R. W. Fu and Y. Q. Zeng, *J. Phys. Chem. C*, 2007, **111**, 2040–2043.
31 D. C. Wu, Z. H. Li, Y. R. Liang, X. Q. Yang, X. H. Zeng and R. W. Fu, *Carbon*, 2009, **47**, 916–918.
32 U. Heudorf, V. Mersch-Sundermann and E. Angerer, *Int. J. Hyg. Environ. Health*, 2007, **210**, 623–634.
33 S. Takeuchi, M. Iida, S. Kobayashi, K. Jin, T. Matsuda and H. Kojima, *Toxicology*, 2005, **210**, 223–233.
34 Z. Y. Ryu, J. T. Zheng, M. Z. Wang and B. J. Zhang, *Carbon*, 1999, **37**, 1257–1264.
35 M. L. Occelli, J. P. Olivier, J. A. Perdigon-Melon and A. Auroux, *Langmuir*, 2002, **18**, 9816–9823.
36 J. H. Park, S. K. Kim, H. S. Kim, Y. J. Cho, J. Park, K. E. Lee, C. W. Yoon, S. W. Nam and S. O. Kang, *Chem. Commun.*, 2013, **49**, 10832–10834.
37 C. Donati, M. Drikas, R. Hayes and G. Newcombe, *Water Res.*, 1994, **28**, 1735–1742.
38 P. Pendleton, R. Schumann and S. H. Wong, *J. Colloid Interface Sci.*, 2001, **240**, 1–8.
39 A. L. Linsebiger, G. Q. Lu and J. T. Yates Jr, *Chem. Rev.*, 1995, **95**, 735–758.
40 S. Sakthivel, M. C. Hidalgo, D. W. Bahnermann, S. U. Geissen, V. Murugesan and A. Vogelpohl, *Appl. Catal., B*, 2006, **63**, 31–40.
41 J. H. Im, S. J. Yang, C. H. Yun and C. R. Park, *Nanotechnology*, 2012, **23**, 035604.
42 M. R. Hoffmann, S. T. Martin, W. Choi and D. F. Bahnemann, *Chem. Rev.*, 1995, **95**, 69–96.
43 J. H. Sun, X. L. Wang, J. Y. Sun, R. X. Sun, S. P. Sun and L. P. Qiao, *J. Mol. Catal. A: Chem.*, 2006, **260**, 241–246.
44 J. Shi, *Chem. Rev.*, 2013, **113**, 2139–2181.
45 I. J. Morales, J. S. González, P. M. Torres and A. J. López, *Appl. Catal., B*, 2011, **105**, 199–205.